Acoustically Driven Fluid and Particle Motion in Confined and Leaky Systems

Rune Barnkob, Nitesh Nama, Liqiang Ren, Tony Jun Huang, Francesco Costanzo, and Christian J. Kähler

Phys. Rev. Applied **9**, 014027 — Published 25 January 2018

DOI: 10.1103/PhysRevApplied.9.014027

Acoustically-driven fluid and particle motion in confined and leaky systems

Rune Barnkob[a*], Nitesh Nama[b], Liqiang Ren[b], Tony J. Huang[c], Francesco Costanzo[b], and Christian J. Kähler[a]
[(a)] *Institute of Fluid Mechanics and Aerodynamics, Bundeswehr University Munich, 85577 Neubiberg, Germany*
[(b)] *Department of Engineering Science and Mechanics, The Pennsylvania State University, University Park, PA 16802, USA*
[(c)] *Department of Mechanical Engineering and Materials Science, Duke University, Durham, NC 27708, USA*

The acoustic motion of fluids and particles in confined and acoustically-leaky systems is receiving increasing attention for its use in medicine and biotechnology. Currently a number of contradicting physical and numerical models exist but their validity is uncertain due to the unavailability of hard-to-access experimental data for validation. We provide experimental benchmarking data by measuring 3D particle trajectories and demonstrate that the particle trajectories can be described numerically without any fitting parameter by a reduced-fluid model with leaky impedance wall conditions. The results reveal the hitherto unknown existence of a pseudo-standing wave that drives the acoustic streaming as well as the acoustic radiation force on suspended particles.

*Corresponding author: barnkob@unibw.de

PACS numbers: 43.25.Nm, 43.25.Qp, 47.35.Rs, 85.50.-n

I. INTRODUCTION

The propagation of acoustic waves in fluids has intrigued researchers for a long time [1]. The classical treatment of the associated phenomena has largely been limited to simple, idealized geometries and in comparison, little attention has been given to the combination of acoustics and fluidics in closed geometries. While there have been many recent reports on the physics in confined resonant chambers [2–5], the physical understanding of acoustically-driven fluid and particle motion in confined leaky systems is limited. These systems are characterized by an acoustic impedance mismatch, between wall material and fluid, that allows a large fraction of the acoustic waves in the fluid to be transmitted to the walls, thereby precluding the build up of acoustic resonances. An often-used realization of such systems is the actuation of a polymer-walled microchannel or microchamber by surface acoustic waves (SAWs) generated on a piezoelectric substrate [6–9]. The SAWs leak energy into the microchannel according to Huygens-Fresnel principle [10] and create an oscillatory pressure distribution which generates second-order effects such as acoustic streaming and acoustic radiation forces [11–13]. Even though there are many reports on their use for applications of fluid and particle manipulation, many basic physical aspects of such systems are yet to be understood. Especially, the following important questions are unanswered: What are the exact three-dimensional oscillatory pressure and velocity fields generated in such systems? Which precise acoustic streaming flows and acoustic radiation forces on suspended particles do they generate? What is the critical particle size for which particles can be manipulated *via* the acoustic radiation forces before they feel a dominating drag from the acoustic streaming flow? Recently, several numerical models have attempted to answer these questions [14–19]. Some reported models represent the polymer walls with hard or leaky boundary conditions [14–17], while others solve the full set of constitutive equations [18, 19], albeit either neglecting the typically large viscous wall damping or by overlooking the importance of wall thickness. The validity of the assumptions and approximations is not evident due to the lack of precise measurement of quantities such as particle motion subject to radiation and streaming-drag forces. Consequently, the models lead to different and at times even contradictory predictions, which are left unvalidated due to the difficult to determine quantitative experimental data of the full three-dimensional phenomena in systems with a single optical access. Specifically, we remark that the direction of the streaming flow observed experimentally in our current work is opposite to the earlier reported numerical predictions [14–16, 20]. This error in the direction of the streaming direction is further transmitted to the calculation of particle trajectories, resulting in wrong numerical predictions for critical particle transition size.

Noting this, the aim of this work is two-fold: Firstly, to make available an experimentally-measured data set that will serve as a benchmark for theoretical models of acoustically-driven confined and leaky systems. Secondly, to provide a simple theoretical framework that correctly captures the three main ingredients: (*i*) constitutive equations for the fluid, (*ii*) boundary conditions, and (*iii*) kinematical framework in which the boundary conditions are transparently enforced in the model. Combining the experimental validation and a reduced-fluid numerical model, we aim to provide an experimentally validated mathematical model as well as an experimentally measured data set against which the future numerical models can be validated.

The article is organized as follows: Section II de-

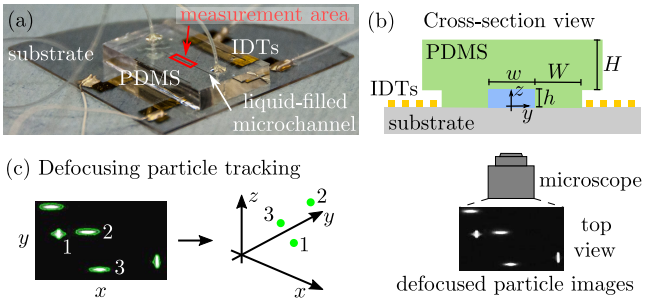

Figure 1. Experimental model system and 3D acquisition of particle trajectories. (a) The model system is a standing SAW microchip consisting of a liquid-filled PDMS microchannel on a lithium niobate piezoelectric substrate acoustically actuated by two IDTs. The microchannel has width $w = 600$ µm, height $h = 125$ µm, and has PDMS wall thickness $W, H = 5$ mm. (b) Sketch of the microchip cross-section showing the optical access through the transparent piezoelectric substrate. (c) The 3D particle positions are determined from the defocused particle images using the General Defocusing Particle Tracking technique.

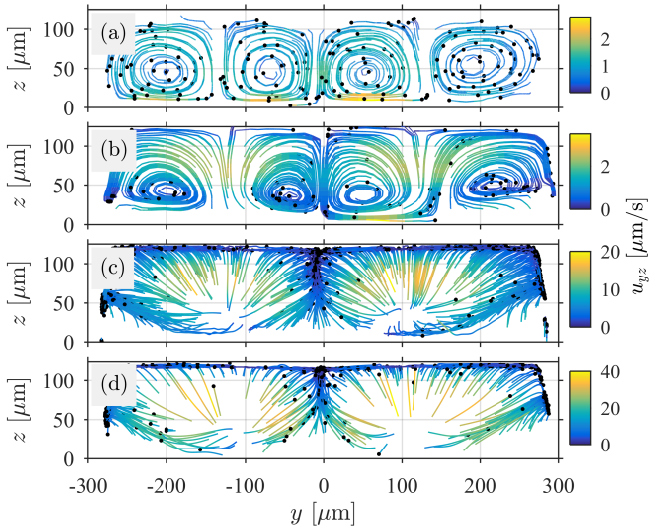

Figure 2. Acoustophoretic particle trajectories along the yz microchannel cross section for increasing particle diameter (a) 0.5 µm, (b) 1.2 µm, (c) 5.2 µm, and (d) 7.8 µm. The velocity magnitudes u_{yz} are indicated by colors (from minimum blue to maximum yellow).

scribes the investigated experimental model system and the experimentally-measured particle trajectories for different particle sizes. Section III gives a physical overview of a general polymer-walled, acoustically-actuated system as well as the nature of the acoustic waves and forces that drive the resulting fluid and particle motion. Section IV outlines the numerical model framework and model system employed and presents the resulting numerical predictions for the acoustic waves as well the particle trajectories for different particle sizes. The numerical predictions of the acoustophoretic particle trajectories and acoustic streaming field are compared against the experimental results in Section II A. Finally, Section V provides a discussion of the results as well as an outlook for future directions.

II. EXPERIMENTAL MODEL SYSTEM

The experimental model system is shown in Fig. 1(a-b): A standing SAW microchip consisting of a straight, liquid-filled, polydimethylsiloxane (PDMS) microchannel of width $w = 600$ µm, height $h = 125$ µm, and PDMS wall thickness $W, H = 5$ mm. The microchannel is bonded on a transparent piezoelectric 128° YX lithium niobate substrate ($LiNbO_3$) deposited with a set of two inter-digital transducers (IDTs). The IDTs have 150 µm finger width and distance and were electrically-actuated at frequency $f = 6.166$ MHz and at peak-peak voltage $U_{pp} = 40$ V, resulting in a standing acoustic wave below the microchannel of wavelength 600 µm. The microchannel was filled with a neutrally-buoyant liquid suspension of fluorescent polystyrene particles in a 20:80 glycerol/water mixture. We investigated the motion of particles of diameters $2a$: 0.5 µm, 1.2 µm, 5.2 µm, and 7.8 µm. No flow was imposed during acoustic actuation and the acoustophoretic particle motion was observed through the substrate with an epi-fluorescent upright microscope, see Fig. 1(b). By using a fully-automated filling, actuation, and image acquisition system [21], we performed for each particle size 20-30 repeated reproducible measurements of low-concentration particle suspensions. All experimental details including chip fabrication and dimensions, and apparatuses are listed in Appendix A.

A. Acoustophoretic particle trajectories

The three dimensional particle trajectories were obtained using the General Defocusing Particle Tracking (GDPT) method, where the depth position z was determined based on the shape of the defocused particle images, see the illustration in Fig. 1(c) [22–24]. The measured particle trajectories are shown in Fig. 2 for increasing particle sizes ranging from 0.5-µm particles in Panel (a) to 7.8-µm particles in Panel (d) [25]. The translationally invariant particle trajectories are shown in the yz cross-section and the colors indicate the yz velocity magnitude u_{yz}. The particle motion shows qualitatively different behavior depending on the particle size. The motion of the 0.5-µm particles in Panel (a) is entirely dominated by the acoustic streaming drag shown by four distinct flow rolls, while the motion of 5.2-µm and 7.8-µm particles in Panel (c) and (d), respectively, is dominated by the acoustic radiation force pushing them to the microchannel top and bottom and to the vertical lines at the substrate displacement nodes at y equal to $-w/2$, 0, and $+w/2$. The motion of the 1.2-µm particles in Panel

(b) shows strong influence from both the streaming drag as well as from the acoustic radiation force — this is characterized by a superposition of the motion of the 0.5-µm and 5.2-µm particles.

III. PHYSICAL DESCRIPTION

The physical picture behind the observed acoustophoretic particle motion is illustrated in Fig. 3(a). When the IDTs are subjected to a harmonic electric actuation, they create two counter-propagating SAWs of wavelength $\lambda_s = c_s/f = 600$ µm, where $c_s = 3994\ \mathrm{m\,s^{-1}}$ is the substrate speed of sound. Consequently, the two SAWs interfere constructively below the microchannel resulting in a standing SAW of wavelength λ_s in the substrate. The SAWs are so-called Rayleigh waves that are restricted to the surface and decay exponentially into the substrate with a penetration depth of typically 1-2 wavelengths [26, 27]. The surface waves are characterized by different displacements in different directions, resulting in an elliptical motion of the surface particles. Upon encountering the PDMS-substrate or fluid-substrate interface, the incoming waves leak energy into the PDMS or the fluid, respectively. The waves undergo refraction at the respective interfaces and move along a direction given by the refraction angle, $\theta = \cos^{-1}(c_m/c_s)$ with respect to the horizontal direction, where c_m represents the speed of sound in the material it is being refracted into.

Apart from the direct interaction with the microchannel, the acoustic waves can undergo damping and can enter the microchannel in several ways, see the sketch in Fig. 3(b). The waves entering the PDMS can be transmitted to the microchannel or can undergo transmission/reflection at the PDMS-air interface, and can again re-enter the microchannel directly or after undergoing further reflections. Similarly, the waves that enter the microchannel directly can be transmitted/reflected at the fluid-PDMS interface. The sound intensity transmission and reflection coefficients from the water/glycerol mixture to the PDMS walls are 0.94 and 0.06, respectively, while they are ≈ 0 and ≈ 1 from PDMS to air. Thus, the PDMS walled systems, characterized by small yet non-zero reflection at fluid-PDMS interface, can be thought of as an intermediate case of the two limiting cases: (*i*) a hard-walled system, characterized by perfect reflections at fluid-wall interfaces resulting in a purely standing wave inside the microchannel, and (*ii*) a fully leaky system, characterized by perfect transmission at the fluid-wall interfaces resulting in a purely traveling wave inside the microchannel. As a result, the oscillating pressure field developed inside the microchannel in a PDMS walled system is a combination of a standing and a traveling wave, which we refer to as a pseudo-standing wave. The pseudo-standing wave can be understood as a traveling wave with position-dependent amplitude, such that the maximum amplitude of the wave changes as the wave moves towards the upper wall. Thus, the oscillating pressure field inside the microchannel is a standing wave horizontally, while in the vertical direction it behaves as a pseudo-standing wave, arising out of the interference between traveling waves propagating upwards and the smaller-amplitude waves reflected from the fluid-PDMS and PDMS-air interfaces. The numerical results revealing this acoustic field will be discussed in Section IV B.

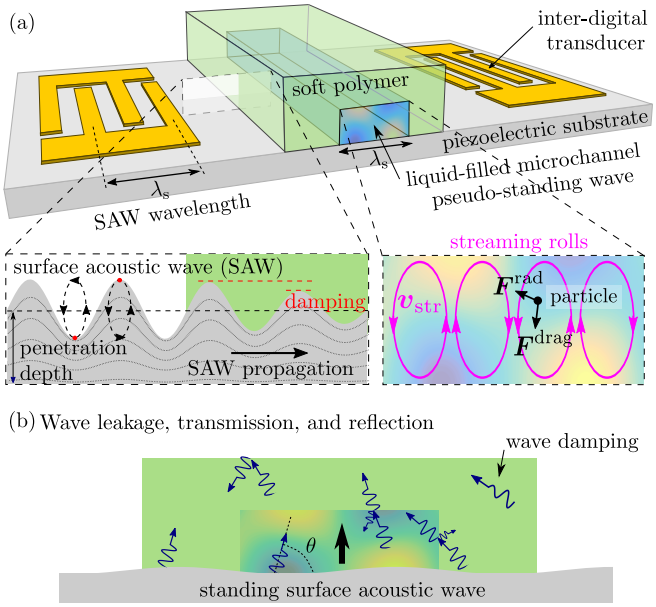

Figure 3. Acoustically-driven fluid and particle motion in a confined and leaky system. The specific sketch takes origin in the investigated experimental model system consisting of a microfluidic channel in a soft polymer actuated by surface acoustic waves, see Fig. 1. The surface acoustic waves leak energy into the polymer and microchannel and as a consequence, a pseudo-standing wave field arises. This field leads to acoustic streaming drag forces and radiation forces on suspended microparticles. (b) The pseudo-standing wave field is a product of several waves entering the microchannel directly or through reflections at material interfaces.

The oscillatory acoustic field in the microchannel leads to time-averaged second-order effects which have consequences for the fluid and particle behavior. Due to viscous attenuation of the acoustic waves, a steady acoustic streaming flow $\boldsymbol{v}_{str}$ is generated. The streaming flow acts on suspended particles via the viscous drag force $\boldsymbol{F}^{drag}$ and in addition, the suspended particles are subject to the primary acoustic radiation force $\boldsymbol{F}^{rad}$ arising due to wave scattering at the particle-liquid interfaces. Since these forces scale differently with particle radius, a ($\boldsymbol{F}^{rad} \propto a^3$, $\boldsymbol{F}^{drag} \propto a$), a particle transition size exists where the particle motion goes from being acoustic streaming dominated to being acoustic radiation force dominated. However, both of these forces scale quadratically with the substrate actuation amplitude ζ_0 and hence neither the particle transition size nor the particle trajectories depend on the displacement amplitude (and hence

the IDT actuation voltage) for neutrally buoyant particles where gravity is negligible.

IV. NUMERICAL FRAMEWORK

The experimental particle trajectories in Fig. 2 are evidently translational invariant along the 1.5-mm measurement section along x (red rectangle in Fig. 1(a)) and thus we model only the 2D particle motion in the yz microchannel cross section. The full physical picture includes interplay of elastic, electromagnetic, and hydrodynamic effects, but in this work we will show that the treatment of a reduced-fluid model is sufficient to describe the experimental findings. In this model only the fluid domain is considered and the acoustic actuation is modeled *via* a pre-described displacement function at the substrate interface while the PDMS boundaries are modeled *via* impedance boundary conditions [15]. As a result, the model considers only the reflections at the fluid-PDMS interface and assumes that all waves traveling through the PDMS are damped enough to be neglected. Based on the damping coefficient of PDMS, this assumption is physically reasonable for PDMS walls that are thicker than ~ 2 mm for waves of frequency larger than 6 MHz [15, 28].

To model the acoustic phenomena inside the microchannel, we adopt a time-scale separation approach, which is based on a generalized Lagrangian formulation [29]. Here the fluid displacement is assumed to be composed of a mean displacement and an oscillating first-order displacement. Contrary to the usually employed Eulerian approaches [15, 30, 31], this approach employs a perturbation expansion of variables defined on the mean configuration rather than the true deformed configuration to provide a mathematically rigorous time-scale separation as well as precise boundary conditions for the first- and second-order subproblems. This distinction is significant since it is reasonable to assume that the channel walls, on average, are not displaced by the harmonic actuation and hence can be assumed to be fixed in the mean configuration. Therefore, unlike the Eulerian approaches where the second-order velocity boundary condition at the oscillating walls is obtained via a Taylor series expansion, the second-order boundary conditions in this formulation are *exact*. In contrast to the previously reported Eulerian approaches, this formulation provides a rigorous and transparent time-averaging method resulting in a time-independent flow at second order. Moreover, since the acoustic streaming is usually visualized by tracking the motion of tracer beads, the formulation of the second-order problem in terms of the mean Lagrangian flow velocity allows direct comparison with the experiments, thereby precluding the need for any postprocessing associated with the conversion of Eulerian flow description to Lagrangian flow description via the notion of Stokes drift. This is favorable from a numerical viewpoint since the Stokes drift depends on the gradients of the first-order field that are difficult to capture precisely in the thin boundary layer. Noting these advantages, we adopt the generalized Lagrangian formulation, and extend it to include the thermoviscous response of the fluid by considering the acoustic perturbations in shear and bulk viscosities as described in [32]. The thermoviscous correction changes the streaming significantly and is significant for capturing correctly the experimental particle trajectories. A comparison of the streaming velocity for the cases with and without thermoviscous corrections can be found in Fig. 5 in the SM [33]. Lastly, the particle trajectories are obtained by assuming a quasi-equilibrium motion of particle under the action of an acoustic streaming-induced hydrodynamic drag $\boldsymbol{F}^{\mathrm{drag}}$ and the radiation force $\boldsymbol{F}^{\mathrm{rad}}$ [30, 34]. We employ the expression for the radiation force given by Karlsen and Bruus [12] and note that this expression provides the radiation force experienced by a particle much smaller than the acoustic wavelength in the limit of a single-particle and therefore any particle-particle interactions are neglected. Further details about the governing equations and the calculation of the numerical particle trajectories are provided in Appendix B.

A. Numerical model system

The model system considered in this work is same as the one considered previously by Nama *et al.* [15]. Specifically, the computational domain consists of a rectangular microchannel of width $w = 600$ μm and height $h = 125$ μm, where the fluid-PDMS boundaries are modeled with leaky impedance boundary conditions and where the SSAW displacement profile at the substrate-fluid interface is obtained by superimposing the displacement profile of two SAWs traveling in opposite directions with a phase difference of π for the z-component

$$\zeta_y(t,y) = 0.6\zeta_0 \left\{ e^{-C_{\mathrm{d}}(w/2+y)} e^{\mathrm{i}\left[2\pi(y-w/2)/\lambda_{\mathrm{s}}-\omega t\right]} + e^{-C_{\mathrm{d}}(w/2-y)} e^{\mathrm{i}\left[2\pi(w/2-y)/\lambda_{\mathrm{s}}-\omega t\right]} \right\}, \tag{1a}$$

$$\zeta_z(t,y) = \zeta_0 \left\{ e^{-C_{\mathrm{d}}(w/2+y)} e^{\mathrm{i}\left[2\pi(y-w/2)/\lambda_{\mathrm{s}}-\omega t-\pi/2\right]} + e^{-C_{\mathrm{d}}(w/2-y)} e^{\mathrm{i}\left[2\pi(w/2-y)/\lambda_{\mathrm{s}}-\omega t-\pi/2+\pi\right]} \right\}, \tag{1b}$$

where ζ_y and ζ_z are the displacements along the y and z direction, respectively, ζ_0 is the substrate displacement

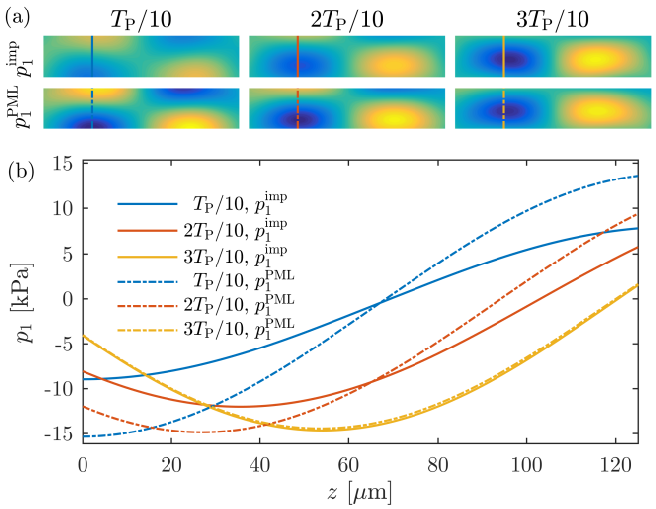

Figure 4. Numerically-obtained first-order pressure field p_1 for two cases: (*i*) Leaky impedance boundary condition on all fluid-PDMS interfaces (imp) and (*ii*) perfectly-matched layer (PML) boundary condition on all fluid-PDMS interfaces to allow full transmission of the waves. (a) Color plots of p_1 (from minimum blue to maximum yellow) for three time instants (Case *i* as top row and Case *ii* as bottom row). (b) Lineplot of p_1 as a function of z for $y = -150$ µm indicated by lines in (a). The pressure amplitude was set through the displacement amplitude ζ_0 fitted via the experiments as explained in Section IV B.

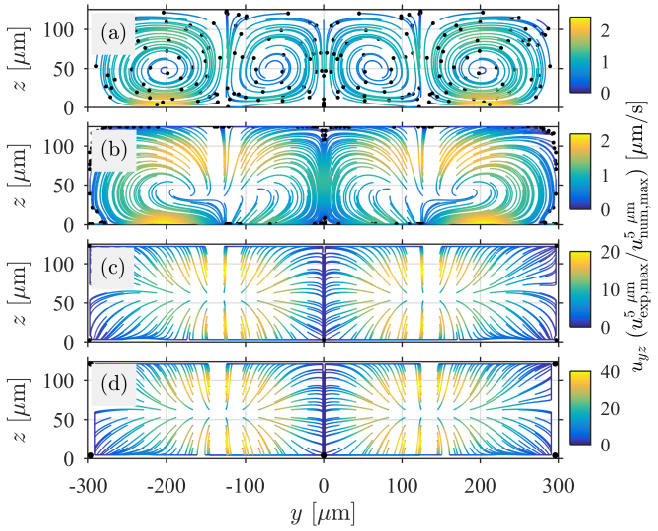

Figure 5. Numerical predictions of the acoustophoretic particle trajectories shown in Fig. 2 for particles of (a) 0.5 µm, (b) 1.2 µm, (c) 5.2 µm, and (d) 7.8 µm. The velocity magnitudes u_{yz} are indicated by colors (from minimum blue to maximum yellow) and are set by fitting the substrate displacement amplitude ζ_0 *via* the 5.2-µm-particle measurements such that the maximum velocity magnitude matches.

amplitude, C_d is the decay coefficient, and $\omega = 2\pi f$ is the angular frequency. We remark here that a typo exists in the similar expression employed in Nama *et al.* [15]. We use the wavelength $\lambda_s = 600$ µm, which gives a predicted frequency of 6.67 MHz for a substrate speed of sound $c_s = 3994$ m s^{-1}. Furthermore, we stress that the actuation profile is based on SAW waves. The experimentally-used substrate is however thin (500 µmcompared to a 600 µmSAW wavelength) and the substrate oscillations might not decay fully before reaching the substrate bottom and reflections can occur. This can further lead to the simultaneous actuation of lamb waves, but for the excited frequency, we assume a negligible alternation of the displacement profile as the observed particle motion (and thus the displacement) is translational invariant along the channel direction x.

For the second-order problem, we set the second-order Lagrangian velocity to zero at all the channel boundaries. We note that this boundary condition is different from those employed previously by Nama *et al.* [15], where the second-order Eulerian velocity was set to zero at all the channel boundaries. As discussed by Nama *et al.* [29], this choice has significant consequences with regards to the mass conservation at the second-order level and results in different directions for the acoustic streaming flow.

B. Numerical predictions

We employ the numerical model to investigate the nature of the first-order acoustic fields setup inside the microchannel. Figure 4 shows three time instants (in terms of a full period of oscillation T_P) of the numerically-obtained first-order pressure field p_1 for two cases: (*i*) Leaky impedance boundary condition on all fluid-PDMS interfaces and (*ii*) perfectly-matched layer (PML) boundary condition on all fluid-PDMS interfaces to allow full transmission of the waves. Panel (a) shows the color plot of the pressure field (case *i* as top row and case *ii* as bottom row), while Panel (b) shows the pressures as a function of z for $y = -150$ µm (indicated by lines in Panel(a)). Case *ii* with PML condition at the walls shows a pure traveling wave characterized by a constant maximum amplitude as it propagates to and through the top wall. In contrast, Case *i* with impedance condition at the walls shows a pseudo-standing wave identified by its varying maximum amplitude as it propagates towards the top wall. As mentioned earlier, since the impedance of PDMS is slightly different from that of the carrier fluid, this is expected as a part of the acoustic waves that travel to the fluid-PDMS interface will be reflected back into the channel. It is this pressure field that drives the motion of the suspended particles via the streaming drag and the acoustic radiation force.

In Figure 5 we show the numerical predictions of the acoustophoretic particles trajectories. The velocity magnitudes u_{yz} are set through the pre-described displacement function by the substrate displacement am-

plitude ζ_0, which is experimentally unknown. However, by comparing the maximum particle velocities for the 5-μm particle trajectories, we can indirectly determine $\zeta_0 = 1.3$ nm for a 40-V actuation, which is used to set the numerical u_{yz} values. The experimentally determined ζ_0 was used to set the scale of pressure in Fig. 4. The trajectories themselves are independent of ζ_0 and therefore are calculated without any fitting parameters. The predictions are qualitatively in good agreement for all particle sizes with the experimental data in Fig. 2. The chosen second-order boundary conditions capture the acoustic streaming direction correctly in Fig. 2(a), but while the maximum streaming velocities are located at the inner rolls near the substrate experimentally, they are located at the outer rolls near the substrate numerically. Furthermore, the model correctly predicts the transition around the 1.2-μm trajectories to the radiation-dominated motion for the larger 5.20-μm and 7.76-μm particles. The radiation-dominated motion is well-predicted with small discrepancies, i.e., experimentally, the particles are pushed away from the two points at $(y, z) = (\pm 120, 40)$, while numerically the two particle depletion points are located at $(y, z) = (\pm 120, 60)$. In addition, the experimental radiation-driven motion scales nearly with the expected particle size squared $(7.76\ \mu\text{m}/5.20\ \mu\text{m})^2 = 2.2$, namely $u_{\max}^{7.8\ \mu\text{m}}/u_{\max}^{5.2\ \mu\text{m}} = 36.3\ \mu\text{m}\,\text{s}^{-1}/21.9\ \mu\text{m}\,\text{s}^{-1} = 1.7$. Here we note that the experimental 7.8-μm particles are few and $36.3\ \mu\text{m}\,\text{s}^{-1}$ is therefore an underestimate of their maximum particle velocity.

In the light of former reports in the literature [18, 19], it is an important finding that the simple reduced-fluid model, which neglects the substrate and wall internal dynamics, predicts the major experimental trends accurately. To test the model even further, we show in Fig. 6 a quantitative comparison of the streaming field $\boldsymbol{v}_{\text{str}}$ (vectors are shown as arrows and magnitudes v_{yz} as colors). Panel (a) shows the measured streaming field $\boldsymbol{v}_{yz}^{\text{exp}}$ from averaging the acoustophoretic velocities of 0.5-μm particles onto a grid consisting of 61×21 square bins of side length 10 μm. The velocity in each bin is calculated from 100-300 independent particles to average out the Brownian motion component, see the details in the SM [33]. Panel (b) shows the numerical representation, where the streaming magnitude is set by the substrate displacement amplitude $\zeta_0 = 1.3$ nm, which was determined by comparing the experimental and numerical 5-μm trajectories. Following, the quantitative, fitting free difference $\Delta v_{yz} = |v_{yz}^{\text{exp}} - v_{yz}^{\text{num}}|$ is shown in Panel (c), displaying local quantitative differences below $1.7\ \mu\text{m}\,\text{s}^{-1}$.

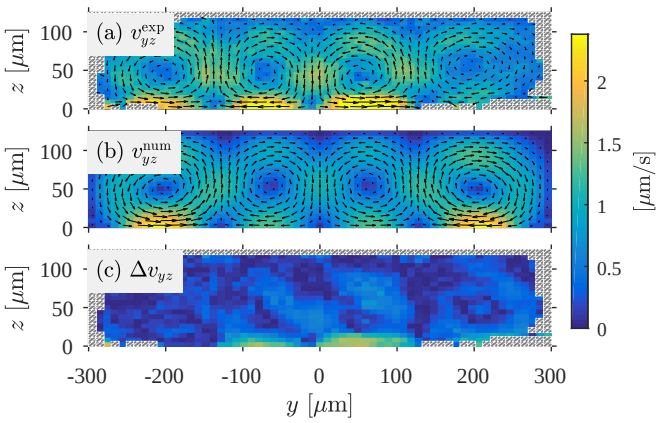

Figure 6. Quantitative comparison of the acoustic streaming field in the SAW microchip (vectors $\boldsymbol{v}_{yz}$ as arrows and velocity magnitudes v_{yz} as colors). The streaming velocity is shown in the vertical yz cross section of the microchannel, divided into an array of 61×21 square bins of side length 10 μm. (a) Experimental velocity field v_{yz}^{exp} obtained from averaging the acoustophoretic velocities of 0.5-μm particles in a 1.5-mm section along the channel direction x. (b) Numerical streaming velocity field v_{yz}^{num}, where the magnitude is set by the substrate displacement amplitude $\zeta_0 = 1.3$ nm determined from experiments. (c) Quantitative difference $\Delta v_{yz} = |v_{yz}^{\text{exp}} - v_{yz}^{\text{num}}|$ of the measured and calculated acoustic streaming field.

V. DISCUSSIONS

The presented quantitative experimental measurements and the reduced-fluid numerical model reveal the nature of fluid and particle motion in SAW-based confined leaky systems. The model predicts correctly the acoustophoretic particle trajectories without any fitting parameters as well as the acoustic streaming direction and amplitude. The product is a fully-validated model with predictions that agree quantitatively very well with the experimental findings. The results reveal the hitherto unknown particle trajectories and dispel the current ambiguities in the literature concerning the streaming direction as well as the critical particle transition size [14, 15, 17–19]. Further, through a combination of the numerical and experimental results, we have predicted the pseudo-standing first-order fields p_1 as well as the substrate displacement amplitude ζ_0. The discrepancies between measurements and model might be attributed to the fact that the considered experimental system has a substrate thickness of 500 μm, which is less than the SAW wavelength of $\lambda_{\text{s}} = 600$ μm. The substrate surface oscillations therefore might not decay fully before reaching the substrate bottom and the Rayleigh-wave assumption in the pre-described displacement $\boldsymbol{\zeta}$ might not be entirely accurate.

The numerical model employed in the current work is a simple reduced-fluid model that aims to characterize fluid and particle motion in acoustically-actuated confined and leaky systems. The reduced-fluid model with its reasonable accuracy, coupled with its simplicity and lower computational costs, offers utility to gain physical insights into the mechanisms that govern particle and fluid motion inside these systems. However, we remark that while the reduced-fluid model provides a good physical understanding of the system, some of the associated assump-

tions can be removed to obtain even deeper physical insights. For instance, more sophisticated models including the channel wall (with the associated viscoelastic damping) and substrate modeling (to better characterize the actuation displacement profile) can be expected to yield more accurate results. One of the primary challenges in the development of such models is to obtain meaningful material parameters for PDMS at the range of frequencies considered. Another significant challenge is the additional computational costs associated with high frequency systems, resulting in smaller boundary layers necessitating smaller mesh sizes. Such a model, with appropriate experimental measurements for validation, can provide interesting physical insights on the effect of channel wall thickness.

ACKNOWLEDGMENTS.

This work was supported by the German Research Foundation (DFG), under the individual grant program KA 1808/16, and by the National Science Foundation CBET-1438126.

Appendix A: Experimental details

1. Standing SAW microchip

The standing SAW microchip is shown in Fig. 1 and all dimensions are listed in Table I. It consists of a PDMS microchannel bonded on a transparent and piezoelectric lithium niobate ($LiNbO_3$) substrate. The PDMS microchannel is straight, with a 600×125 μm^2 cross section, and one inlet and one outlet. The thickness of the microchannel walls is $W, H = 5$ mm. The piezoelectric substrate is acoustically-actuated by two interdigital transducers (IDTs) on each side of the microchannel with a distance of 12 mm. The IDTs each consist of two comb-shaped arrays of pairs of gold electrodes with 150 μm wide fingers with a inter-distance of 150 μm.

Device fabrication. The standing SAW microchip was fabricated by bonding the PDMS-based microchannel onto the lithium niobate ($LiNbO_3$) substrate. The PDMS microchannel was made from a 10:1 PDMS and curing agent mixture and the channels were fabricated using standard soft-lithography procedures. The IDT gold electrodes were deposited on the substrate by standard photo lithography and lift-off processes.

2. Experimental setup

In order to obtain several particle trajectories while maintaining a low particle concentration (to neglect particle interactions), the standing SAW microchip was experimentally investigated using a fully-automated system similar to the system presented by Augustsson *et al.* [21]. The system enables, in a automatic fashion, the acquisition of several repeated stop-flow acoustophoretic measurements in a reproducible manner. In one experimental cycle the system fills a particle suspension into the microchip, starts/stops the flow, starts/stops recording of the microchannel, starts/stops the acoustic actuation, logs acoustic driving voltages, and saves the recorded images to disk. For each experimental cycle the driving frequencies, driving voltages, and channel positions can be varied.

Acoustic actuation. The standing SAW microchip was acoustically driven with a function generator (GW Instek AFG-2125, Taiwan) and an in-house built amplifier from the group of Laurell, Lund University. The peak-peak voltage U_{pp} was read off using an oscilloscope (TDS2001C, Tektronix, OR, USA). The standing SAW microchip was actuated at frequency $f = 6.166$ MHz and at peak-peak voltages $U_{\mathrm{pp}} \sim 40$ V.

Flow setup. The standing SAW microchip was filled with particle suspension using a syringe pump (PHD Ultra, Harvard Apparatus GmbH, MA, USA) and stop-flow mode was obtained by short-circuiting the microchannel via a switching valve (Rheodyne MXX777-601, IDEX-HS, WA, USA).

Imaging. The acoustophoretic particle motion in the microchannel was observed using an epi-fluorescent upright microscope (Axio Imager.Z2 ACR, Carl Zeiss Microscopy GmbH, Germany) equipped with a 10x/0.3 magnification lens. The microchannel was illuminated using continuous diode-pumped laser with 2 W at 532 nm wavelength (www.mylaserpage.de, Germany). The images of fluorescent particles were recorded using a sCMOS camera (16-bit, 2560×2160 pixels, PCO GmbH, Germany). The entire measurement volume was $1500 \times 700\times200$ μm^3. In order to avoid polarized particle images due to polarization in the substrate we used a circular polarizer between the microscope and camera sensor. Furthermore, a cylindrical lens of focal length $f_{\mathrm{cyl}} = 300$ mm was used in order to obtain astigmatic particle images convenient for obtaining the 3D particle position [24].

Particle suspensions. The investigated microparticle suspension consisted of fluorescent polystyrene particles (Microparticles GmbH, Germany) suspended in a 20:80 glycerol/water mixture, see the material parameters in Table II. Four particle sizes were investigated, namely particles of diameter 0.537 μm, 1.2 μm, 5.20 μm,

Table I. Standing SAW microchip dimensions.

Parameter	Symbol	Value	Unit
SSAW microchip dimensions			
Microchannel width	w	600	μm
Microchannel height	h	125	μm
PDMS wall thickness	W, H	5	mm
Substrate thickness	–	500	μm
IDT electrode finger width	–	150	μm
IDT electrode finger distance	–	150	μm
IDT pair inter-distance	–	12	mm

and 7.76 μm. The specific mixture was chosen for neutral buoyancy, such that gravity could be neglected in comparison to the acoustically-driven motion. The particle suspensions were tested for neutral buoyancy. The 0.5 μm- and 1 μm-diameter particles did not sediment, while the 5 μm- and 8 μm-diameter particles had measured sedimentation velocities of $(0.10\pm0.01)\ \mu\mathrm{m\,s^{-1}}$ and $(0.13\pm0.01)\ \mu\mathrm{m\,s^{-1}}$, respectively.

General defocusing particle tracking. The full three-dimensional particle trajectories were obtained from the defocused particle images. The defocused particle images were processed using the General Defocusing Particle Tracking (GDPT) technique and the GDPTlab Matlab implementation [22, 23]. In short, the GDPT method relies on a set of calibration particle images for which the depth position is known for a given particle image shape. A target particle is then compared to the set of calibration images thus giving the depth coordinate.

Appendix B: Numerical formulation

1. Governing equations

Here, we provide details concerning the numerical formulation, its implementation as well as particle trajectory calculation strategy. The fluid is considered to be linear, viscous, and compressible and is governed by the standard balance laws for mass, momentum, and energy [35], given as

$$\dot{\rho} + \rho\boldsymbol{\nabla}\cdot\boldsymbol{v} = 0, \tag{B1}$$
$$\rho(\dot{\boldsymbol{v}} - \boldsymbol{b}) - \boldsymbol{\nabla}\cdot\boldsymbol{\sigma} = \boldsymbol{0}, \tag{B2}$$
$$\rho T\dot{s} - \boldsymbol{\nabla}\cdot(k_{\mathrm{th}}\boldsymbol{\nabla}T) = \boldsymbol{0}, \tag{B3}$$

where ρ is the mass density distribution, $\boldsymbol{v}$ is the velocity, s is the entropy, T is the temperature, $\boldsymbol{b}$ is the external body force density per unit mass, $\boldsymbol{\sigma}$ is the Cauchy stress, k_{th} is the thermal conductivity, and a dot over a variable indicates the material time derivative of that variable. Here, all the fields are understood to be a function of time t and the position $\boldsymbol{y}$ in the current (or deformed) configuration.

For a linear, viscous, Newtonian, compressible fluid, the constitutive response function for the Cauchy stress is given by

$$\boldsymbol{\sigma} = -p(\rho)\boldsymbol{I} + \mu(\boldsymbol{\nabla}\boldsymbol{v} + \boldsymbol{\nabla}\boldsymbol{v}^{\mathrm{T}}) + \mu^{\mathrm{b}}(\boldsymbol{\nabla}\cdot\boldsymbol{v})\boldsymbol{I}, \tag{B4}$$

where p is the fluid (static) pressure, μ and μ^{b} represent the shear and bulk viscosities, respectively, and $\rho(p,T)$ is assumed to be the following linear relation

$$\rho = \rho_0(\gamma\kappa_0 p - \alpha_p T), \tag{B5}$$

where ρ_0, γ, κ_0, and α_p are constants denoting the fluid's density, heat capacity ratio, compressibility, and thermal expansion coefficient at rest, respectively. Furthermore, we use

$$Tds = c_p dT - \frac{\alpha_p T}{\rho}dp, \tag{B6}$$

where c_p is the heat capacity and α_p is the thermal expansion coefficient. To consider the change in fluid properties due to the variation of temperature and density, we write the acoustic perturbations in shear and bulk viscosities as [32]

$$\mu(T,\rho) = \mu_0(T_0,\rho_0) + \mu_1(T_0,T_1,\rho_0,\rho_1), \tag{B7}$$
$$\mu_1 = \Big(\frac{\partial\mu}{\partial T}\Big)_{T=T_0}T_1 + \Big(\frac{\partial\mu}{\partial\rho}\Big)_{\rho=\rho_0}\rho_1, \tag{B8}$$
$$\mu^{\mathrm{b}}(T,\rho) = \mu_0^{\mathrm{b}}(T_0,\rho_0) + \mu_1^{\mathrm{b}}(T_0,T_1,\rho_0,\rho_1), \tag{B9}$$
$$\mu_1^{\mathrm{b}} = \Big(\frac{\partial\mu^{\mathrm{b}}}{\partial T}\Big)_{T=T_0}T_1 + \Big(\frac{\partial\mu^{\mathrm{b}}}{\partial\rho}\Big)_{\rho=\rho_0}\rho_1, \tag{B10}$$

where the values for the various constants can be found in Table II.

Following Nama *et al.* [29], we reformulate the governing equations onto the mean configuration and employ a time-scale separation approach. Henceforth, all the flow variables refer to the flow variables mapped onto the mean configuration and these variables are understood to be functions of time t and position $\boldsymbol{x}$ in the mean configuration of the fluid. The time-scale separation results in a linearization of the above system of governing equations into two sets of linear equations, which are referred to as the first-order and the second-order equations. The first-order system of equations, also referred to as the acoustic subproblem, is given by

$$\partial_t\rho_1 + \rho_0\boldsymbol{\nabla}\cdot\boldsymbol{v}_1 = 0, \tag{B11}$$
$$\rho_0\partial_t\boldsymbol{v}_1 - \boldsymbol{\nabla}\cdot\boldsymbol{P}_1 = \boldsymbol{0}, \tag{B12}$$
$$\rho_0 c_p\partial_t T_1 - \alpha_p T_0\partial_t p_1 - k_{\mathrm{th}}\nabla^2 T_1 = 0, \tag{B13}$$

where

$$\boldsymbol{P}_1 = -c_0^2\rho_1\boldsymbol{I} + \mu\Big(\boldsymbol{\nabla}\boldsymbol{v}_1 + \boldsymbol{\nabla}\boldsymbol{v}_1^{\mathrm{T}}\Big) + \mu^{\mathrm{b}}\big(\boldsymbol{\nabla}\cdot\boldsymbol{v}_1\big)\boldsymbol{I}. \tag{B14}$$

Similarly, the second-order set of equations, also referred to as the mean dynamics subproblem, is given by

$$\boldsymbol{\nabla}\cdot\boldsymbol{v}_2 = 0 \quad\text{and}\quad \boldsymbol{\nabla}\cdot\langle\boldsymbol{P}_2\rangle = \boldsymbol{0}, \tag{B15}$$

Table II. Material parameters at $T = 25$ ℃.

Parameter	Symbol	Value	Unit
80 % water, 20 % glycerol (weight percentage)			
Density[36]	ρ_0	1.050×10^3	$\mathrm{kg\,m^{-3}}$
Speed of sound[37]	c_0	1.588×10^3	$\mathrm{m\,s^{-1}}$
Shear viscosity[36]	μ	1.525×10^0	mPa s
Bulk viscosity[a]	μ^{b}	2.485×10^0	mPa s
Compressibility[b]	κ_0	3.78×10^2	$\mathrm{TPa^{-1}}$
Thermal conduct. [38]	k_{th}	5.22×10^{-1}	$\mathrm{W\,m^{-1}\,K^{-1}}$
Heat capacity[c]	c_p	3.83×10^3	$\mathrm{J\,kg^{-1}\,K^{-1}}$
Thermal diffusivity[f]	D_{th}	1.30×10^{-7}	$\mathrm{m^2\,s^{-1}}$
Thermal expansion [39]	α_p	4.639×10^{-4}	$\mathrm{K^{-1}}$
Heat capacity ratio[d]	γ	1.011×10^0	
Thermodyn. deriv.[e]			
	$\frac{1}{\mu}\frac{\partial \mu}{\partial T}$	-2.57×10^{-2}	$\mathrm{K^{-1}}$
	$\frac{1}{\mu}\frac{\partial \mu}{\partial \rho}$	-3.472×10^{-4}	$\mathrm{kg^{-1}m^3}$
	$\frac{1}{\mu_{\mathrm{b}}}\frac{\partial \mu_{\mathrm{b}}}{\partial T}$	-2.584×10^{-2}	$\mathrm{K^{-1}}$
Lithium niobate ($LiNbO_3$)			
Density [40]	ρ_{sub}	4.648×10^3	$\mathrm{kg\,m^{-3}}$
Sound speed[41]	c_{sub}	3.994×10^3	$\mathrm{m\,s^{-1}}$
Therm. conduct. [42]	$k_{\mathrm{th}}^{\mathrm{sub}}$	4×10^0	$\mathrm{W\,m^{-1}\,K^{-1}}$
Heat capacity [42]	c_p^{sub}	6.33×10^2	$\mathrm{J\,kg^{-1}\,K^{-1}}$
Decay coefficient [15]	C_{d}	116	$\mathrm{m^{-1}}$
Thermal diffusivity [f]	$D_{\mathrm{th}}^{\mathrm{sub}}$	1.4×10^{-6}	$\mathrm{m^2\,s^{-1}}$
Poly-dimethylsiloxane (PDMS, 10:1)			
Density [43]	ρ_{wall}	9.20×10^2	$\mathrm{kg\,m^{-3}}$
Sound speed, long. [28]	$c_{\mathrm{wall}}^{\mathrm{L}}$	1.077×10^3	$\mathrm{m\,s^{-1}}$
Sound speed, trans. [44]	$c_{\mathrm{wall}}^{\mathrm{T}}$	1.00×10^2	$\mathrm{m\,s^{-1}}$
Atten. coeff. [g][28]		7.14×10^2	$\mathrm{m^{-1}}$
Therm. conduct. [45]	$k_{\mathrm{th}}^{\mathrm{wall}}$	1.5×10^{-1}	$\mathrm{W\,m^{-1}\,K^{-1}}$
Heat capacity [45]	c_p^{wall}	1.460×10^3	$\mathrm{J\,kg^{-1}\,K^{-1}}$
Thermal diffusivity [f]	$D_{\mathrm{th}}^{\mathrm{wall}}$	1.1×10^{-7}	$\mathrm{m^2\,s^{-1}}$
Polystyrene			
Density [46]	ρ_{p}	1.050×10^3	$\mathrm{kg\,m^{-3}}$
Sound speed[h][47]	c_{p}	2.350×10^3	$\mathrm{m\,s^{-1}}$
Poisson's ratio [48]	σ_{p}	3.5×10^1	
Compressibility[i]	κ_{p}	2.49×10^2	$\mathrm{TPa^{-1}}$

[a] Value for water used [49].

[b] Calculated as $\kappa_0 = 1/(\rho_0 c_0^2)$.

[c] The heat capacity c_p for the solution is calculated as $c_p = 0.2c_p^{\mathrm{gl}} + 0.8c_p^{\mathrm{wa}}$, where $c_p^{\mathrm{gl}} = 2.41 \times 10^3$ J kg^{-1} K^{-1} ([ref]) is the heat capacity of glycerol and where $c_p^{\mathrm{wa}} = 4.18 \times 10^3$ J kg^{-1} K^{-1} ([ref]) is the heat capacity of water. This approximation assumes that the molecular interaction of the two liquids has no effect on each other's heat capacity.

[d] Value for water used [32].

[e] Thermodynamic derivatives:
$\frac{1}{\mu}\frac{\partial \mu}{\partial T}$ is calculated from $\mu(T)$ [36].
$\frac{1}{\mu}\frac{\partial \mu}{\partial \rho}$ is taken as that of water [32].
$\frac{1}{\mu_{\mathrm{b}}}\frac{\partial \mu_{\mathrm{b}}}{\partial T}$ is taken as that of water [32].

[f] Calculated as $D_{\mathrm{th}} = k_{\mathrm{th}}/(\rho c_p)$ [50].

[g] Calculated at 6.65 MHz via law fit to data by Tsou *et al.*[28].

[h] At 20 ℃.

[i] Calculated as $\kappa_{\mathrm{p}} = \frac{3(1-\sigma_{\mathrm{p}})}{1+\sigma_{\mathrm{p}}}\frac{1}{(\rho_{\mathrm{p}} c_{\mathrm{p}}^2)}$ [51].

with

$$\begin{aligned}\langle \boldsymbol{P}_2 \rangle = &-\langle q \rangle \boldsymbol{I} + \mu\Big[\boldsymbol{\nabla} \boldsymbol{v}_2 + \boldsymbol{\nabla} \boldsymbol{v}_2^{\mathrm{T}}\Big] \\ &+ \tfrac{1}{2} c_0^2 \rho_0 \Big\langle (\boldsymbol{\nabla}\cdot\boldsymbol{\xi})^2 - \boldsymbol{\nabla}\boldsymbol{\xi}^{\mathrm{T}} : \boldsymbol{\nabla}\boldsymbol{\xi} \Big\rangle \boldsymbol{I} \\ &+ \mu^{\mathrm{b}} \Big\langle (\boldsymbol{\nabla}\cdot\boldsymbol{\xi})(\boldsymbol{\nabla}\cdot\boldsymbol{v}_1) - \boldsymbol{\nabla}\boldsymbol{\xi}^{\mathrm{T}} : \boldsymbol{\nabla}\boldsymbol{v}_1 \Big\rangle \boldsymbol{I} \\ &+ \mu \Big\langle \boldsymbol{\nabla}\cdot\boldsymbol{\xi}\Big(\boldsymbol{\nabla}\boldsymbol{v}_1 + \boldsymbol{\nabla}\boldsymbol{v}_1^{\mathrm{T}}\Big) \\ &- \boldsymbol{\nabla}\boldsymbol{v}_1 \boldsymbol{\nabla}\boldsymbol{\xi} - \boldsymbol{\nabla}\boldsymbol{\xi}^{\mathrm{T}} \boldsymbol{\nabla}\boldsymbol{v}_1^{\mathrm{T}} \Big\rangle \\ &- \Big\langle \Big[c_0^2 \rho_0 (\boldsymbol{\nabla}\cdot\boldsymbol{\xi})\boldsymbol{I} + \mu\Big(\boldsymbol{\nabla}\boldsymbol{v}_1 + \boldsymbol{\nabla}\boldsymbol{v}_1^{\mathrm{T}}\Big) \\ &+ \mu^{\mathrm{b}} (\boldsymbol{\nabla}\cdot\boldsymbol{v}_1)\boldsymbol{I}\Big] \boldsymbol{\nabla}\boldsymbol{\xi}^{\mathrm{T}} \Big\rangle + \Big\langle \mu_1^{\mathrm{b}} (\boldsymbol{\nabla}\cdot\boldsymbol{v}_1)\boldsymbol{I} \\ &+ \mu_1 \Big(\boldsymbol{\nabla}\boldsymbol{v}_1 + \boldsymbol{v}_1^{\mathrm{T}}\Big) \Big\rangle \end{aligned} \tag{B16}$$

where $q(\boldsymbol{x}, t)$ is a scalar Lagrange multiplier that is determined by enforcing the constraint in the first of Eqs. (B15), $\boldsymbol{\xi}$ is the first-order fluid displacement, and $\boldsymbol{v}_2$ is the Lagrangian streaming velocity $\boldsymbol{v}_{\mathrm{str}}$ that will be used for obtaining the particle trajectories. Here, $\langle A \rangle$ denote the time average of the quantity A over one period of oscillation. At the second-order level, the energy equation is de-coupled from the balance of mass and balance of momentum equation, and therefore we choose to only solve the balance of mass and momentum equations. However, we remark that the terms containing μ_1 and μ_1^{b} do appear in the above expression due to the consideration of variation of viscosities with respect to temperature and density. We also remark that the second-order system of equations obtained in this formulations is *inherently* time-independent as opposed to the previously employed Eulerian approaches wherein a time-dependent second-order problem is obtained for which steady solutions are typically sought. The above system of equations, complemented with appropriate boundary conditions at respective orders, can be solved successively.

2. Numerical particle trajectories

To obtain numerical predictions of particle trajectories inside the microfluidic channel, we consider a dilute particles suspension of neutrally-buoyant particles so as to neglect the gravitational force as well as particle-particle interactions, both hydrodynamic and acoustic. Thus, the motion of the particle is dictated by an acoustic radiation force $\boldsymbol{F}^{\mathrm{rad}}$ and an acoustic streaming induced hydrodynamic drag force $\boldsymbol{F}^{\mathrm{drag}}$. Considering an immersed particle of radius a that is much smaller than the wavelength in the fluid λ_0, mass density ρ_{p}, and compressibility κ_{p}, the radiation force is given by Karlsen and Bruus [12]

$$\boldsymbol{F}^{\mathrm{rad}} = -\pi a^3 \left[\frac{2\kappa_0}{3} \mathrm{Re}[f_1^* p_1^* \nabla p_1] - \rho_0 \mathrm{Re}[f_2^* \boldsymbol{v}_1^* \cdot \nabla \boldsymbol{v}_1] \right], \tag{B17}$$

where p_1 and $\boldsymbol{v}_1$ are the first-order pressure and velocity, respectively, $\kappa_0 = 1/(\rho_0 c_0^2)$ is the compressibility of the liquid, $\mathrm{Re}[A]$ denotes the real part of quantity A, the asterix denotes complex conjugates, and the coefficients f_1 and f_2 are given by

$$f_1 = 1 - \frac{\kappa_\mathrm{p}}{\kappa_0} \quad \text{and} \quad f_2 = \frac{2(\rho_\mathrm{p} - \rho_0)}{2\rho_\mathrm{p} + \rho_0}. \tag{B18}$$

Note that we neglect in f_2 the thermoviscous corrections, which are small for hard particles with densities similar to the fluid. For polystyrene particles in a 20:80 glycerol/water suspensions (see material parameters in Table II), $f_2 = 0.0343 + 0.0001\mathrm{i}$ when including thermoviscous corrections while $f_2 = 0.0342$ when thermoviscous corrections are neglected. Note that this is the general expression for the radiation force without *a priori* assumption of whether we deal with traveling or standing waves. On the other hand, the drag force is proportional to $\boldsymbol{u} - \boldsymbol{v}_\mathrm{str}$, which is the particle velocity $\boldsymbol{u}$ relative to the streaming velocity $\boldsymbol{v}_\mathrm{str} = \boldsymbol{v}_2$. When wall effects are negligible, the drag force is estimated *via* the simple formula $\boldsymbol{F}^\mathrm{drag} = 6\pi\mu a\big(\boldsymbol{v}_\mathrm{str} - \boldsymbol{u}\big)$. The motion of the particle is then predicted *via* the application of Newton's second law

$$m_\mathrm{p}\frac{\mathrm{d}\boldsymbol{u}}{\mathrm{d}t} = \boldsymbol{F}^\mathrm{rad} + \boldsymbol{F}^\mathrm{drag}, \tag{B19}$$

where m_p is the mass of the particle. In many acoustofluidics problems the inertia of the particle can be neglected since the characterstic time of acceleration is small in comparison to the time scale of the motion of the particles [52]. Doing so, Eq. (B19) can be solved for $\boldsymbol{u}$

$$\boldsymbol{u} = \boldsymbol{v}_\mathrm{str} + \frac{\boldsymbol{F}^\mathrm{rad}}{6\pi\mu a}. \tag{B20}$$

3. Numerical implementation

Next, we provide the details of the numerical implementation. For the first-order acoustic subproblem, we seek time-harmonic solutions for the velocity, density, and temperature of the form

$$\boldsymbol{v}_1(\boldsymbol{x}, t) = \boldsymbol{v}_1(\boldsymbol{x})e^{\mathrm{i}\omega t}, \tag{B21a}$$

$$\rho_1(\boldsymbol{x}, t) = \rho_1(\boldsymbol{x})e^{\mathrm{i}\omega t}, \tag{B21b}$$

$$T_1(\boldsymbol{x}, t) = T_1(\boldsymbol{x})e^{\mathrm{i}\omega t}, \tag{B21c}$$

where $\boldsymbol{v}_1(\boldsymbol{x})$, $\rho_1(\boldsymbol{x})$, and $T_1(\boldsymbol{x})$ are time independent complex-valued fields of space only. As noted earlier, for the second-order problem, the energy equation is decoupled from the balance of mass and momentum equations. Since we are only interested in fluid and particle motion, we choose to solve only the balance of mass and momentum equations at the second order. Since the second-order momentum equation is solved with pure Dirichlet boundary conditions on all boundaries, we assign a zero average pressure constraint to admit a unique solution. We adopt the standard approach of using a composite element with proven stability properties, such as $\mathcal{P}2$-$\mathcal{P}3$, where $\mathcal{P}2$ and $\mathcal{P}3$ represent triangular elements with Lagrange polynomials for the pressure and the velocity fields of order 2 and 3, respectively. All the numerical solutions presented in this article were obtained for two-dimensional problems via the commercial finite element software COMSOL Multiphysics [53]. We have used COMSOL as a high-level programming environment to create our own implementation of the problems in question using the *Weak PDE* interface. For both the first- and second-order problems, we used a direct solver provided in COMSOL. Our numerical results indicate a singularity in the gradients of the first-order fields, thereby precluding a conventional mesh convergence analysis, see the details in the SM [33]. Therefore, to ascertain the convergence of our numerical results with respect to changes in the mesh size, we performed numerical simulations on a series of meshes where the maximum element size in the bulk of the domain was chosen to be 2 μm, while progressively decreasing the size of the boundary mesh, d_b. We observe the fields away from the bottom left and right corners and found that decreasing the mesh size beyond $d_\mathrm{b} = 0.3\delta$ does not change the results significantly, and therefore throughout the rest of this work, we use $d_\mathrm{b} = 0.3\delta$ where $\delta = \sqrt{\frac{2\mu}{\omega\rho_0}}$ is the boundary layer width.

[1] J. Lighthill, *Waves in Fluids* (Cambridge University Press, 2002).

[2] B. Vanherberghen, O. Manneberg, A. Christakou, T. Frisk, M. Ohlin, H. M. Hertz, B. Onfelt, and M. Wiklund, "Ultrasound-controlled cell aggregation in a multi-well chip," Lab on a Chip **10**, 2727–2732 (2010).

[3] C. R. P. Courtney, C.-K. Ong, B. W. Drinkwater, P. D. Wilcox, C. Demore, S. Cochran, P. Glynne-Jones, and M. Hill, "Manipulation of microparticles using phase-controllable ultrasonic standing waves," The Journal of the Acoustical Society of America **128**, EL195–EL199 (2010).

[4] P. B. Muller, M. Rossi, Á. G. Marín, R. Barnkob, P. Augustsson, T. Laurell, C. J. Kähler, and H. Bruus, "Ultrasound-induced acoustophoretic motion of microparticles in three dimensions," Physical Review E **88**, 023006 (2013).

[5] A. Lamprecht, S. Lakämper, T. Baasch, I. A. T. Schaap, and J. Dual, "Imaging the position-dependent 3D force on microbeads subjected to acoustic radiation forces and streaming," Lab on a Chip **16**, 2682–2693 (2016).

[6] T. Franker, A. R. Abate, D. A. Weitz, and A. Wixforth, "Surface acoustic wave (saw) directed droplet flow in microfluidics for pdms devices," Lab on a Chip **9**, 2625–2627 (2009).

[7] G. Destgeer and H. J. Sung, "Recent advances in microfluidic actuation and micro-object manipulation via surface acoustic waves," Lab on a Chip **15**, 2722–2738 (2015).

[8] D. J Collins, B. Morahan, J. Garcia-Bustos, C. Doerig, M. Plebanski, and A. Neild, "Two-dimensional single-cell patterning with one cell per well driven by surface acoustic waves," Nature communications **6** (2015).

[9] S. Li, F. Ma, H. Bachman, C. E. Cameron, X. Zeng, and T. J. Huang, "Acoustofluidic bacteria separation," Journal of Micromechanics and Microengineering **27**, 015031 (2016).

[10] C. Devendran, D. J. Collins, Y. Ai, and A. Neild, "Huygens-fresnel acoustic interference and the development of robust time-averaged patterns from traveling surface acoustic waves," Physical Review Letters **118**, 154501 (2017).

[11] N. Riley, "Steady streaming," Annual Review of Fluid Mechanics **33**, 43–65 (2001).

[12] J. T. Karlsen and H. Bruus, "Forces acting on a small particle in an acoustical field in a thermoviscous fluid," Physical Review E **92**, 043010 (2015).

[13] J. T. Karlsen, P. Augustsson, and H. Bruus, "Acoustic force density acting on inhomogeneous fluids in acoustic fields," Physical Review Letters **117**, 114504 (2016).

[14] J. Guo, Y. Kang, and Y. Ai, "Radiation dominated acoustophoresis driven by surface acoustic waves," Journal of colloid and interface science **455**, 203–211 (2015).

[15] N. Nama, R. Barnkob, Z. Mao, C. J. Kähler, F. Costanzo, and T. J. Huang, "Numerical study of acoustophoretic motion of particles in a pdms microchannel driven by surface acoustic waves," Lab on a Chip **15**, 2700 (2015).

[16] Z. Mao, Y. Xie, F. Guo, L. Ren, P.-H. Huang, Y. Chen, J. Rufo, F. Costanzo, and T. J. Huang, "Experimental and numerical studies on standing surface acoustic wave microfluidics," Lab on a chip **16**, 515–524 (2016).

[17] F. Guo, Z. Mao, Y. Chen, Z. Xie, J. P. Lata, P. Li, L. Ren, J. Liu, J. Yang, M. Dao, *et al.*, "Three-dimensional manipulation of single cells using surface acoustic waves," Proceedings of the National Academy of Sciences **113**, 1522–1527 (2016).

[18] A. N.Darinskii, M. Weihnacht, and H. Schmidt, "Computation of the pressure field generated by surface acoustic waves in microchannels," Lab on a Chip **16**, 2701–2709 (2016).

[19] N. R. Skov and H. Bruus, "Modeling of microdevices for saw-based acoustophoresis — a study of boundary conditions," Micromachines **7**, 182 (2016).

[20] C. Devendran, T. Albrecht, J. Brenker, T. Alan, and A. Neild, "The importance of travelling wave components in standing surface acoustic wave (ssaw) systems," Lab on a Chip **16**, 3756–3766 (2016).

[21] P. Augustsson, R. Barnkob, S. T. Wereley, H. Bruus, and T. Laurell, "Automated and temperature-controlled micro-piv measurements enabling long-term-stable microchannel acoustophoresis characterization," Lab on a Chip **11**, 4152–4164 (2011).

[22] R. Barnkob, C. J. Kähler, and M. Rossi, "General defocusing particle tracking," Lab on a Chip **15**, 3556–3560 (2015).

[23] GDPTlab, "Matlab implementation of the general defocusing particle tracking," Universität der Bundeswehr München (https://www.unibw.de/lrt7/gdpt).

[24] C. Cierpka, R. Segura, R. Hain, and C. J. Kähler, "A simple single camera 3c3d velocity measurement technique without errors due to depth of correlation and spatial averaging for microfluidics," Measurement Science and Technology **21**, 045401 (2010).

[25] The 0.5-µm and 1.2-µm trajectories were slow and have been filtered for Brownian motion by calculating the trajectories from a binned velocity field averaged from several repeated measurements, see the details in the SM [33].

[26] J. David N. Cheeke, *Fundamentals and Applications of Ultrasonic Waves* (CRC Press LLC, 2002).

[27] M. Gedge and M. Hill, "Acoustofluidics 17: Theory and applications of surface acoustic wave devices for particle manipulation," Lab on a Chip **12**, 2998–3007 (2012).

[28] J. K Tsou, J. Liu, A. I. Barakat, and M. F. Insana, "Role of ultrasonic shear rate estimation errors in assessing inflammatory response and vascular risk," Ultrasound in medicine & biology **34**, 963–972 (2008).

[29] N. Nama, T. J. Huang, and F. Costanzo, "Acoustic streaming: An arbitrary lagrangian-eulerian perspective," Journal of Fluid Mechanics **825**, 600–630 (2017).

[30] P. B. Muller, R. Barnkob, M. J. H. Jensen, and H. Bruus, "A numerical study of microparticle acoustophoresis driven by acoustic radiation forces and streaming-induced drag forces," Lab on a Chip **12**, 4617–4627 (2012).

[31] D. Köster, "Numerical simulation of acoustic streaming on surface acoustic wave-driven biochips," SIAM Journal on Scientific Computing **29**, 2352–2380 (2007).

[32] P. B. Muller and H. Bruus, "A numerical study of thermoviscous effects in ultrasound-induced acoustic streaming in microchannels," Physical Review E **90**, 043016 (2014).

[33] "See supplemental material at [url will be inserted by publisher] for the paper acoustically-driven fluid and particle motion in confined and leaky systems.".

[34] R. Barnkob, P. Augustsson, T. Laurell, and H. Bruus, "Acoustic radiation- and streaming-induced microparticle velocities determined by microparticle image velocimetry in an ultrasound symmetry plane," Physical Review E **86**, 056307 (2012).

[35] M. E. Gurtin, E. Fried, and L. Anand, *The Mechanics and Thermodynamics of Continua* (Cambridge University Press, New York, 2010).

[36] N.-S. Cheng, "Formula for the viscosity of a glycerol- water mixture," Industrial & engineering chemistry research **47**, 3285–3288 (2008).

[37] F. A. A. Fergusson, E. W. Guptill, and A. D. MacDonald, "Velocity of sound in glycerol," The Journal of the Acoustical Society of America **26**, 67–69 (1954).

[38] O. K. Bates, "Binary mixtures of water and glycerol," Industrial & Engineering Chemistry **28**, 495–498 (1936).

[39] D. M. Cristancho, D. R. Delgado, F. Martínez, M. A. A. Fakhree, and A. Jouyban, "Volumetric properties of glycerol + water mixtures at several temperatures and correlation with the jouyban-acree mode," Revista Colombiana de Ciencias Químico - Farmacéuticas **40**, 92–115 (2011).

[40] S. C. Abrahams and P. Marsh, "Defect structure dependence on composition in lithium niobate," Acta Crystal-

lographica Section B **42**, 61–68 (1986).
[41] S. K. Sankaranarayanan and V. R. Bhethanabotla, "Numerical analysis of wave generation and propagation in a focused surface acoustic wave device for potential microfluidics applications," IEEE transactions on ultrasonics, ferroelectrics, and frequency control **56**, 631–643 (2009).
[42] V. V. Zhdanova, V. P. Klyuev, V. V. Lemanov, I. A. Smirnov, and V. V. Tikhonov, "Thermal properties of lithium niobate crystals," Soviet Physics Solid state, USSR **10**, 1360 (1968).
[43] D. Armani, C. Liu, and N. Aluru, "Re-configurable fluid circuits by pdms elastomer micromachining," in *Micro Electro Mechanical Systems, 1999. MEMS'99. Twelfth IEEE International Conference on* (Ieee, 1999) pp. 222–227.
[44] E. L. Madsen, H. J. Sathoff, and J. A. Zagzebski, "Ultrasonic shear wave properties of soft tissues and tissue-like materials," The Journal of the Acoustical Society of America **74**, 1346–1355 (1983).
[45] J. Mark, *Polymer Data Handbook* (Oxford Univ Press, New York, 1999).
[46] CRCnetBASE Product, *CRC Handbook of Chemistry and Physics*, 92nd ed. (Taylor and Francis Group, www.hbcpnetbase.com/, 2012).
[47] L. Bergmann, *Der Ultraschall und seine Anwendung in Wissenschaft und Technik*, 6th ed. (S. Hirzel Verlag, Stuttgart, 1954).
[48] P. H. Mott, J. R. Dorgan, and C. M. Roland, "The bulk modulus and poisson's ratio of "incompressible" materials," Journal of Sound and Vibration **312**, 572–575 (2008).
[49] M. J. Holmes, N. G. Parker, and M. J. W. Povey, "Temperature dependence of bulk viscosity in water using acoustic spectroscopy," Journal of Physics: Conference Series **269**, 012011 (2011).
[50] H. Bruus, *Theoretical Microfluidics* (Oxford University Press, Oxford, 2008).
[51] L. D. Landau and E. M. Lifshitz, *Theory of Elasticity. Course of Theoretical Physics*, 3rd ed., Vol. 7 (Pergamon Press, Oxford, 1986).
[52] R. Barnkob, *Physics of Microparticle Acoustophoresis — Bridging Theory and Experiments*, Ph.D. thesis, Danmarks Tekniske Universitet (DTU), Lyngby, Denmark (2012).
[53] COMSOL Multiphysics 5.2a, www.comsol.com, (2016).